Pre-Launch Assessment of RADARSAT Constellation Mission Medium Resolution Modes for Sea Oil Slicks and Lookalike Discrimination

Mohammed Dabboor, Suman Singha, Benoit Montpetit, Benjamin Deschamps & Dean Flett

Published online: 27 Sep 2019.

Submit your article to this journal

Article views: 32

View related articles

View Crossmark data

Taylor & Francis
Taylor & Francis Group

Pre-Launch Assessment of RADARSAT Constellation Mission Medium Resolution Modes for Sea Oil Slicks and Lookalike Discrimination

Mohammed Dabboor[a], Suman Singha[b], Benoit Montpetit[c], Benjamin Deschamps[d], and Dean Flett[d]

[a]Science and Technology Branch, Environment and Climate Change Canada, Government of Canada, Dorval, Quebec H9P 1J3, Canada; [b]Remote Sensing Technology Institute (IMF), German Aerospace Center (DLR), Bremen, Germany; [c]Landscape Science and Technology Division, Environment and Climate Change Canada, Government of Canada, Ottawa, Ontario K1A 0H3, Canada; [d]Canadian Ice Service, Environment and Climate Change Canada, Government of Canada, Ottawa, Ontario K1G 3Z4, Canada

ABSTRACT

The RADARSAT Constellation Mission (RCM) is a Canadian Synthetic Aperture Radar (SAR) mission, providing C-band SAR data continuity of the RADARSAT-1 and RADARSAT-2 satellite missions. The RCM which was recently launched (June 2019) will provide compact polarimetry (CP) as a polarization option for all non-quad-polarization imaging modes. Maritime pollution monitoring is one of the RCM core applications. Thus, the purpose of this study is to provide an initial evaluation of the expected potential of the RCM mission for maritime pollution monitoring. Herein, we investigate simulated CP SAR data of three RCM Medium Resolution (MR) SAR modes for oil slick detection and discrimination from lookalike (LA) features. Results of our study indicated that the steeper radar incidence angle seems to be preferable for oil slick detection in all examined modes. The ScanSAR 50 m resolution (SC50M) mode showed the highest overall performance in terms of LA and Emulsion (EM) classification (95.4%). This was also valid for LA and Crude Oil (CO) classification (96.7%). The performance of the SC50M mode was slightly higher than that of the ScanSAR 30 m resolution (SC30M) mode.

RÉSUMÉ

La Mission Constellation RADARSAT (MCR) est une mission Canadienne de radar à synthèse d'ouverture (RSO), fournissant la continuité des données en bande C des missions satellitaires RADARSAT-1 et RADARSAT-2. La MCR, qui fut lancée récemment (juin 2019) fournira une option de polarisation en polarimétrie compacte (PC) pour tous les modes d'imagerie autres que le mode quad-pol. La surveillance de la pollution maritime est l'une des applications centrales de la MCR. Le but de cette étude est donc de fournir une évaluation initiale du potentiel attendu de la mission MCR pour la surveillance de la pollution maritime. Nous évaluons l'aptitude des données ROS simulées en polarimétrie compacte pour les trois modes MCR de résolution moyenne envers la détection de nappes de pétrole et la discrimination entre les nappes de pétrole et d'autres régions aux signatures similaires. Les résultats indiquent que l'angle d'incidence le plus étroit est préférable pour la détection des nappes de pétrole pour tous les modes examinés. Le mode ScanSAR ayant une résolution de 50 m (SC50M) a obtenu la meilleure performance globale (95.4%) pour classifier les émulsions (EM) et les régions aux signatures similaires (LA) à des nappes de pétrole. Cette performance (96.7%) s'applique également à la classification du pétrole brut (CO) et des régions similaires (LA) à des nappes de pétrole. La performance du mode SC50M est légèrement meilleure que celle du mode ScanSAR ayant une résolution de 30 m (SC30M).

Introduction

Major advancements in the remote sensing techniques for oil slick detection in the ocean have been observed recently (Minchew et al. 2012; Angelliaume et al. 2018; Fingas and Brown 2018). State-of-the-art satellite imagery, especially Synthetic Aperture Radar (SAR), enables to spot oil slicks in the early stages of an accident and to monitor systematic pollution over major shipping routes (Vijayakumar and Santhi 2015). Moreover, the trajectory of the oil slick may be

---

obtained through multi-temporal imagery; thereby assisting in drift prediction modelling that may be used to facilitate clean-up operations and warning systems (Cheng et al. 2014). The backscattered microwave energy of the electromagnetic spectrum from a radar target (e.g. slick-free sea surface) is governed mainly by constructive and destructive interferences of the electromagnetic radar signals, causing the speckle noise (Lee and Pottier 2009). Oil films dampen the capillary waves on the sea surface and thus the backscatter, causing slicks to appear as dark spots in gray tones intensity SAR images, while the surrounding slick-free sea remains relatively brighter (Apel and Jackson 2004). The detectability of oil slicks depends on a number of factors, such as the rheological properties of oil slicks, the speckle noise in SAR imagery, the radar incidence angle and the wind speed (Alpers et al. 2017; Buono et al. 2018; Skrunes et al. 2018; Nunziata et al. 2019). Oil slicks are not the only phenomenon that produces dark spots in SAR images. Common meteorological and oceanographical phenomena that produce similar kind of dark spots in SAR images are referred to as lookalikes (LA). Frequently occurring LA phenomena are low-wind sea surface areas, upwelling and down-welling zones, ocean currents, atmospheric fronts, rain cells and most prominently the presence of algae bloom (Topouzelis 2008). Discrimination between oil slicks and LA still remains a major challenge for implementing automated operational oil slick detection systems.

To distinguish between oil slicks and LA features, a number of automatic and semi-automatic techniques based on single polarization SAR data (traditionally ScanSAR type imagery) have been developed (Topouzelis and Psyllos 2012; Brekke and Solberg 2005; Singha et al. 2013). Some semi-automated methods have been implemented for operational services (Singha et al. 2014). These methods traditionally exploit features, such as patch backscatter, texture, and geometry to discriminate oil slicks and LA. However, such techniques suffer from considerable misclassification rate which is undesirable for operational services. Furthermore, small operational spills from offshore platforms are often ignored as their signature is not captured on traditional ScanSAR images due to their coarser spatial resolution.

Fully polarimetric (FP) SAR imagery is acknowledged as providing high performance in oil slick detection, due to the complete radar target information content (Migliaccio et al. 2015; Zhang et al. 2011; Skrunes et al. 2014; Skrunes et al. 2015), compared to conventional single or dual polarization SAR imagery.

A number of polarimetric features extracted from FP SAR imagery have been proposed for pixel-based oil slick classification (Migliaccio et al. 2015; Skrunes et al. 2014; Singha et al. 2016), which are found to be suitable for oil slick and LA discrimination to a greater extent. A recent study by Singha et al. (2016) proposed a method which exploits a combination of traditional and polarimetric features and yielded considerably better discrimination compared to results obtained using only traditional features (e.g. area, perimeter, complexity, spreading, object standard deviation, maximum and minimum contrast, etc.). A review of polarimetric SAR methods for sea oil slick observation is presented in Migliaccio et al. (2015). Yet current FP SAR systems have reduced swath width with limited range of incidence angles relative to single and dual polarized SAR imagery, and higher system requirements (e.g. power consumption, system complexity, etc.).

A SAR system with compact polarimetric (CP) SAR architecture constitutes a significant advancement in the field of Earth observation using radar remote sensing (Raney 2007). A CP SAR architecture transmits circular (right or left) or 45° oriented linear polarization and receives 2 orthogonal, mutually coherent linear horizontal and vertical polarizations (Raney 2007; Nord et al. 2009; Cloude et al. 2012; Yin et al. 2015; Buono et al. 2016a). Another CP SAR configuration could transmit circular (right or left) polarization and receives 2 mutually coherent right and left circular polarizations. The 3 recently proposed CP SAR configurations for Earth observation could be a compromised choice for SAR applications (Buono et al. 2016a; Buono et al. 2016b; Charbonneau et al. 2010). The main advantage of such SAR systems is that they provide increased radar target information in comparison to standard single and dual polarized SAR systems, while covering much greater swath widths compared to FP SAR systems (Charbonneau et al. 2010). Such SAR architectures were included in the C-band Indian Radar Imaging Satellite (RISAT-1), in the L-band Japanese Advanced Land Observing Satellite (ALOS-2) carrying the Phased Array type L-band Synthetic Aperture Radar (PALSAR-2), and in the RADARSAT Constellation Mission (RCM). The RCM is a Canadian SAR mission which was recently launched (June 2019) with the purpose of supporting the operational use of SAR imagery for different Earth observation applications, including maritime pollution monitoring. The mission, through its three identical satellites, will provide daily revisits of Canada's vast territory and marine regions, as well as daily access to 90% of the world's surface. The nominal orbital altitude of the satellites is 600 km with a revisit

time of 4 days (12 days/satellite). In the CP architecture of the RCM, the antenna transmits a right-hand circularly polarized signal and receives two orthogonal, mutually coherent linear horizontal and vertical polarizations. The CP option is available in all RCM imaging modes, except for the quad-polarization SAR mode (Dabboor et al. 2018a). Ocean surveillance is one of the core RCM applications. Specific imaging modes of medium and low spatial resolutions are dedicated for ice mapping, maritime pollution monitoring, and marine wind estimation. The potential of the RCM with respect to RADARSAT-2 lies in its rapid revisit time and compact polarimetry as new polarization option.

The potential of CP SAR imagery for oil slick monitoring is still an active research area, which is conducted using mainly CP SAR data simulated from FP SAR imagery. Espeseth et al. (2017) compared the performance of simulated CP SAR data for the detection of oil slicks under various conditions to that of FP SAR using polarimetric features. Espeseth et al. (2017) concluded that CP SAR could be an effective alternative to FP SAR for oil slick detection and monitoring. Zhang et al. (2017) confirmed also this conclusion, where ten CP features were extracted from simulated CP SAR data and used in a Support Vector Machine (SVM) classification for the detection of mineral oil slicks. This conclusion was previously highlighted by Buono et al. (2016b). Shirvany et al. (2012) investigated the potential of the degree of polarization feature, while Li et al. (2016) studied the effectiveness of the second element of the Stokes vector from simulated CP SAR data for oil slick detection. The sensitivity of a set of CP features to oil slick, LA, and clean sea surface was investigated in Nunziata et al. (2015). In that study, some CP features such as the polarimetric entropy derived from the simulated CP SAR data were found to exhibit a pronounced sensitivity which could allow for the discrimination between oil slicks, LA, and clean sea surface. In Salberg et al. (2014), a new CP feature similar to the polarimetric coherence feature from FP SAR imagery was derived and proved effective for the discrimination between oil slick and LA caused by low-wind conditions.

Different studies focused on proposing models for pseudo quad-pol reconstruction from CP SAR data, considering different assumptions (Nord et al. 2009; Zhang et al. 2017; Collins et al. 2015; Li et al. 2015; Yin et al. 2015). Nord et al. (2009) studied the degree to which FP SAR data can be approximated by the different CP SAR configurations through the reconstruction of the quad-pol covariance matrix, assuming symmetry

properties of the geophysical media. Sabry and Vachon (2014) explored the links between CP and FP covariance matrices which can be used to examine target property assumptions for various CP configurations. Also, they provided means to explore a priori target property assumptions and their suitability for the pseudo quad-pol covariance matrices reconstruction from CP covariance matrices. Some studies focused on considering assumptions applicable only to ocean surface backscattering for the pseudo quad-pol reconstruction from CP SAR data (Zhang et al. 2017; Collins et al. 2015; Li et al. 2015; Yin et al. 2015). Studies on oil slick detection and monitoring using real CP SAR data are quite limited. This is because the CP SAR architecture of the ALOS-2 satellite is currently on experimental mode and the RISAT-1 CP SAR imagery suffered from high-noise floor up to $-17\,dB$ (Misra et al. 2013) and calibration issues related to the non-circularity of the transmitted radar signals. However, a study by Kumar et al. (2014) assessed the potential of different decomposition methods for oil slick detection using RISAT-1 CP SAR data.

The innovative aspect of this study lies in the fact that it provides the first evaluation of the expected potential performance of compact polarization of all the RCM Medium Resolution (MR) modes for the discrimination between oil slicks and plant oil which is treated as LA. These modes are the StripMap 16 m resolution (16M) mode, the ScanSAR 30 m resolution (SC30M) mode, and the ScanSAR 50 m resolution (SC50M) mode, and are characterized by different Noise Equivalent Sigma Zero (NESZ) or nominal noise floors ($-25\,dB$, $-24\,dB$, and $-22\,dB$, respectively). Simulated CP SAR data were derived and 23 CP features were extracted for each RCM MR mode using 2 RADARSAT-2 FP SAR images acquired during an oil slick exercise in the North Sea. A signal-to-noise analysis was performed on the simulated RCM datasets. Next, a separability analysis based on the Kolmogorov–Smirnov (K-S) distance was conducted to identify those CP features with discrimination capability between LA and oil slicks. The identified CP features were further investigated for possible information redundancy using the Spearman correlation coefficient. Hence, optimal CP vectors were extracted and used as input for the classification of LA and oil slicks in a SVM classification approach. Finally, classification results were analyzed and compared between RCM modes. Since the ultimate objective of this study is to investigate the expected potential of the RCM MR modes for the discrimination between LA and oil slicks, we followed the same procedure indicated in

Skrunes et al. (2014) for masking out ships and clean sea surface. Thus, possible effects of ships and varying sea clutter are avoided in our study. It is worth mentioning that the expected potential of the RCM MR modes for maritime pollution monitoring is of high interest, since for the next few years the RCM will be the only C-band SAR satellite operationally providing CP SAR imagery.

Experimental site and SAR imagery

The experimental site for this study is located in the North Sea offshore Norway. An oil slick exercise by the Norwegian Clean Seas Association for Operating Companies at the Frigg field was conducted in June 2011 and previously reported in (Skrunes et al. 2014). Three different types of oil were discharged at sea; Crude Oil (CO), Emulsion (EM), and plant oil to be treated as LA. The EM was released first, 16 hours before the release of the plant oil. The CO was released 4 hours after the release of plant oil. As stated in Skrunes et al. (2014), the released EM was $20\,m^3$ of Oseberg blend crude oil mixed with 5% intermediate fuel oil with viscosity ≤ 380 cSt. The water content of EM during the released was found to be equal to 69%. A volume of $0.4\,m^3$ of Radiagreen EBO plant oil (a biodegradable lubricant used by the oil industry as an additive to drilling muds) was spilled and left untouched on the surface (Skrunes et al. 2014). An evaporated Balder CO of volume $30\,m^3$ was released. Detailed information about the experimental setup and the released oil slicks is reported in Skrunes et al. (2014).

The released oil was captured by two RADARSAT-2 FP SAR images. The first image shown in Figure 1a (RSa), acquired on 8 June 2011, captured the EM and plant oil during the descending pass of the satellite (the CO was not spilled yet at the time of the satellite pass). The age of the spilled oil slicks at the time of the acquisition of the first RADARSAT-2 image was 18 hours and 2 hours for the EM and plant oil, respectively. The mid-range radar incidence angle of the first image was 46.7°. The second image shown in Figure 1b (RSb) was acquired on the same date and captured all the three released oil types (CO, EM, and plant oil) during a subsequent ascending pass of the satellite. The ages of the oil slicks at the time of the acquisition of the RSb image were 29 hours, 13 hours, and 9 hours, for the EM, plant oil and CO, respectively. The mid-range radar incidence angle of the RSb image was 35.3°. Table 1 summarizes the SAR imagery acquired during the experiment.

The wind at the time of the SAR imagery acquisition for both images was northwest with quite low speed; 1.6–3.3 m/s. In our study, samples of plant oil and mineral oil slicks (Figure 1) were collected based on those indicated in Skrunes et al. (2014). For the rest of the paper, we refer to the released plant oil as LA. Also, as in Skrunes et al. (2014), we refer to the first SAR image as RSa and the second SAR image as RSb.

Methodology

An RCM data simulator developed at the Canada Center for Mapping and Earth Observation is used for the RCM data simulation. The simulator produces simulated SAR products based on the pre-launch specifications provided by the Canadian Space Agency. Specifications such as the spatial resolution, noise floor and number of looks of each mode are considered in the simulation process. The RCM simulator uses as input FP RADARSAT-2 images to simulate RCM data of any of the ten planned RCM modes. The RCM simulator converts the RADARSAT-2 16-bit complex products to 32-bit float complex by applying the sigma-nought calibration coefficients provided. Then, the RH (right circular transmit and linear horizontal receive) and RV (right circular transmit and linear vertical receive) polarizations are calculated from the calibrated HH, HV, VH, and VV polarizations. Based on the RCM product specifications, RH and RV are down-sampled using 2 D fast Fourier transformation techniques to the spatial resolution defined for each beam mode. The RH and RV are converted to Stokes vector, which is then speckle filtered and used for incoherent CP decomposition and feature extraction.

In our study, each RADARSAT-2 image was used to simulate three sets of RCM CP data, corresponding to the 16 M, SC30M and SC50M SAR modes. Specifications of the three RCM modes are presented in Table 2.

For each set of simulated RH and RV channels (RCM deliverable product), the simulator derived 23 CP features which are presented in Table 3. Thus, for the two available RADARSAT-2 images we had a total of six sets of simulated RCM CP features to be analyzed.

The NESZ, which is also called noise floor, is critical in the ability of SAR imagery in detection and classification of oil slicks, and must be lower than the measured normalized radar cross section. Therefore, a noise analysis procedure is applied to the simulated
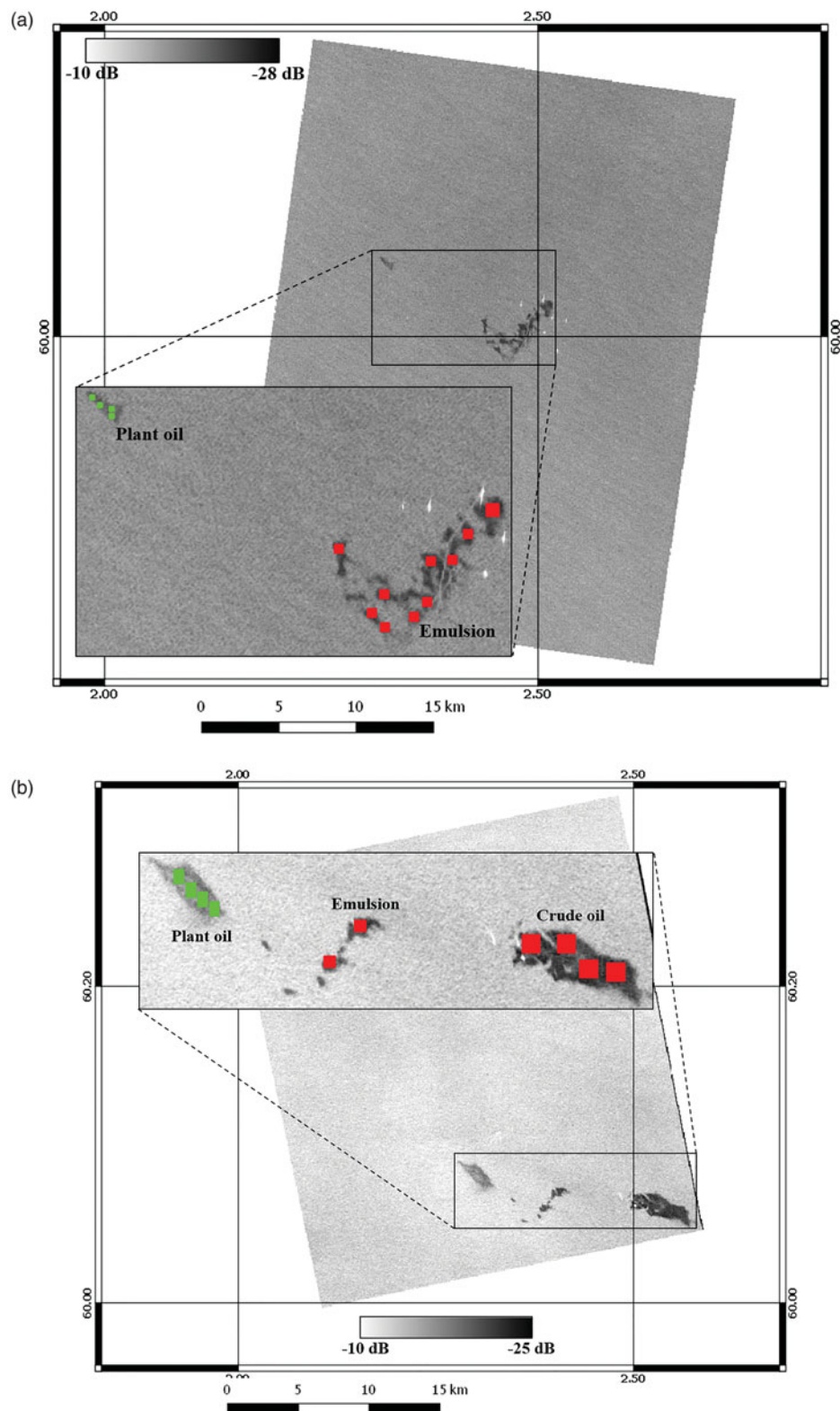
Figure 1. (a) Total backscattering power (named SPAN) of the first RADARSAT-2 image (RSa) with plant oil and emulsion and (b) SPAN of the second RADARSAT-2 image (RSb) with plant oil, emulsion, and crude oil. Green polygons indicate plant oil, while red polygons indicated mineral oil.

Table 1. Summary of SAR image acquisitions.

RADARSAT-2 Beam Mode	Acquisition Date and Time	Orbit Direction	Incidence Angle	Nominal Azimuth Resolution	Nominal Range Resolution
FQ28	08/06/2011 05.59 UTC	Descending	46.7°	7.7m	7.2 m (near range) 7.1 m (far range)
FQ15	08/06/2011 17.27 UTC	Ascending	35.3°	7.7m	9.2 m (near range) 8.8 m (far range)

Table 2. Specifications of the RCM 16M, SC30M, and SC50M SAR modes.

Beam Mode	Nom. Res. (m)	Swath (km)	Number of Looks (range × azimuth)	Noise Floor (dB)
SC50M (ScanSAR)	50	350	4 × 1	−22
SC30M (ScanSAR)	30	125	2 × 2	−24
16M (StripMap)	16	30	1 × 4	−25

Table 3. Assessed features extracted from the simulated RCM CP SAR data.

Short form	Description
SV0, SV1, SV2, SV3	Stokes vector elements (Raney et al. 2012)
SE_Pol, SE_Int	Shannon entropy polarimetric and intensity components (Réfrégier and Morio 2006)
σ^0_{RL}, σ^0_{RR}, σ^0_{RH}, σ^0_{RV}	Sigma naught backscattering—right circular transmit and left circular, right circular, linear horizontal or linear vertical receive polarization (Dabboor and Geldsetzer 2014)
$\sigma^0_{RV}/\sigma^0_{RH}$	Right co-polarized ratio (Lee and Pottier 2009)
ρ_{RHRV}	RH RV correlation coefficient (Dabboor and Geldsetzer 2014)
m-δ_S, m-δ_V, m-δ_DB	Surface, volume, and double bounce scattering from m-δ decomposition (Raney 2007)
m-χ_odd, m-χ_V, m-χ_even	odd, volume, and even bounce scattering from m-χ decomposition (Raney et al. 2012)
m	Degree of polarization (Raney et al. 2012)
δ_{RHRV}	RH RV phase difference (Charbonneau et al. 2010)
μ	Conformity coefficient (Truong-Loi et al. 2009)
$\sigma^0_{RR}/\sigma^0_{RL}$	Circular polarization ratio (Raney 2007)
α_s	Alpha feature related to the ellipticity of the compact scattered wave (Cloude et al. 2012)

RH and RV images, which will be the deliverables of the RCM, to verify that the σ^0_{RH} and σ^0_{RV} backscattering values are higher than the expected nominal noise floor of each RCM mode. It is worth mentioning that the nominal noise floor of each RCM mode shown in Table 2 represents the highest expected noise floor. The actual noise floor value will depend on the radar beam position and the position within the beam swath (Dabboor et al. 2018b). It is worth mentioning that the nominal noise floors of the SC30M and SC50M modes shown in Table 2 are expected to be further improved with the implementation of the stepped receive functionality in the RCM ScanSAR modes. According to the stepped receive functionality, the receive beam is steered in elevation in discrete steps during the receive window, allowing for improved NESZ and range ambiguity levels.

Following the noise analysis, the oil slicks are investigated in a nonparametric approach to avoid any statistical distribution assumption. The first step in our nonparametric approach is the estimation of the separability between LA and mineral oil slicks (EM and CO) in each CP feature using the nonparametric Kolmogorov-Smirnov (K-S) distance. The K-S distance is the maximum absolute difference between 2 cumulative distribution functions (Duda et al. 2000). The K-S distance can take values between 0 and 1.

In this study, we take the CP features with K-S distance between 2 classes >0.5 as features with separability potential. Moderate separability is assumed existing if $0.5 <$ K-S distance <0.7, which becomes good separability if $0.7 \leq$ K-S distance <0.9. We assume a CP feature has very good separability between 2 classes if the K-S distance ≥ 0.9. The selected 0.7 and 0.9 values are reasonable threshold values to define the 3 aforementioned groups and were successfully used in different image processing and feature selection studies (Desbordes et al. 2017; Dabboor et al. 2017, 2018b). In each RCM mode, the analysis of the separability using the K-S distance leads to the identification of CP features with potential separability between LA and mineral oil slicks and the exclusion of those CP features with no separation capability.

Since some of the identified features might be correlated, the next step in our nonparametric analysis approach is the estimation of the correlation between the identified CP features. This step is important since it allows for the detection of possible redundancies between the identified CP features. The correlation between the identified CP features is evaluated using the nonparametric Spearman correlation coefficient R (Press et al. 2007). The Spearman correlation coefficient can take values between −1 and 1. However, in

this study we consider its absolute value, leading to R ranges between 0 and 1. Correlation analysis of the extracted features from the first step allows for the exclusion of possible correlated CP features. In this study, we consider 2 CP features highly correlated if the Spearman correlation value $\geq$ 0.90. The ultimate goal is to obtain a vector of less correlated CP features (R < 0.90) suitable of the classification of LA and mineral oil slicks. We selected the threshold value of 0.9 since it was adopted and successfully used in different feature extraction studies (Geldsetzer et al. 2015, Dabboor et al. 2017, 2018b). The output of the correlation analysis for each RCM mode is a CP vector containing less correlated CP features which are used as input in the SVM classification algorithm for the classification of LA and mineral oil slicks. SVM classification is a machine learning supervised classification technique based on decision planes which define classification decision boundaries (Burges 1998). Half of the collected samples (Figure 1) are randomly selected and used for training the classification algorithm and the other half for the classification accuracy assessment.

Results

Noise analysis

In the RSa image, the signal-to-noise analysis was performed based on the selected sample polygons of LA and EM (Figure 1a). In the 16 M mode, the number of LA and EM samples is 15312 and 44393, respectively. In the SC30M and SC50M modes, the number of LA and EM samples is 1932 and 5489, respectively. Figure 2 shows the mean and standard deviation of the simulated σ_{RH}^0 and σ_{RV}^0 backscattering values for the three RCM Modes in the RSa image.

In Figure 2, the simulated RH and RV signals are seen to fluctuate close to the nominal noise floor of the 16 M (−25 dB, Figure 2a), SC30M (−24 dB, Figure 2b), and SC50M (−22 dB, Figure 2c) RCM modes, with all mean values being below it. In the 16 M mode (Figure 2a), LA has mean RH values 2.4–2.5 dB and mean RV values 0.9–1.6 dB below the noise floor level. EM has mean values 2.5–3.5 dB and 1.1–2.8 dB below the noise floor level of the RH and RV channels, respectively. In the SC30M mode (Figure 2b), LA regions have mean signal values of 2.2–2.4 dB and 0.7–1.8 dB below the noise floor in RH and RV, respectively. In this mode (Figure 2b), mean signal values from EM regions are also below the noise level (-24 dB) in both RH and RV (2.8–3.5 dB and 1.3–3.3 dB, respectively). Similar to 16 M and SC30M

mode, mean values for LA lie below the noise floor of the SC50M mode (Figure 2c) for RH (2.5–3.6 dB) and RV (1.7–2.3 dB). This is also valid for the EM regions which have mean signal values of 2.8–3.8 dB and 1.8–3.6 dB below the noise level (-22 dB) in RH and RV (Figure 2c). These results suggest high noise contamination observed in the simulated RH and RV in all 3 RCM modes. This could be explained by the large incidence angle of the RSa image (46.7°) which decreases the ocean backscattering (Skrunes et al. 2014), confirming the preferred steep incidence angle for oil slick detection (Marghany and Hashim 2011).

Figure 3 shows the mean and standard deviation of the simulated σ_{RH}^0 and σ_{RV}^0 backscattering values for the 3 RCM Modes in the RSb image, calculated from the selected samples in Figure 1b. In the 16 M mode, the number of LA, EM, and CO samples is 88210, 29880, and 143511, respectively. In the SC30M and SC50M modes, the number of LA, EM, and CO samples is 7555, 2567, and 12303, respectively.

For the 16 M mode (Figure 3a), the mean values in the RV channel of LA, EM, and CO are always higher than the mean values in the RH channel. The mean values for LA lie mostly above the noise floor for both RH and RV channels (Figure 3a), whereas the mean values of EM and CO are closer to and sometimes slightly below the noise floor of the 16 M mode (−25 dB). The LA mean values lie 1–1.8 dB above the noise floor for the RH channel and 2.0–2.9 dB above the noise floor for the RV channel. In EM regions, the mean values lie from 0.9 dB below to 0.1 dB above the noise floor of the RH channel and from 0.1–1.0 dB above the noise floor for the RV channel (Figure 3a). In the CO regions, the mean values in the RH channel lie from 0.7 dB below to 0.2 dB above the noise floor, whereas for the RV channel the mean values lie from 0.4 dB below to 0.7 dB above the noise floor (Figure 3a).

Figure 3b shows the RH and RV mean values for LA, EM and CO in the SC30M mode. Similar to the 16 M mode, the mean backscattering values in the RV channel of LA, EM, and CO are always higher than the mean values in the RH channel for the SC30M mode. The mean values for LA lie mostly above the noise floor in both RH and RV channels. For EM and CO, mean values are closer to and sometimes slightly below the noise floor of the SC30M mode (−24 dB). LA mean values range from 1.5–2.5 dB and 2.7–3.6 dB above the SC30M noise level, for RH and RV channels, respectively. In the EM regions, the mean values in the RH channel lie from 0.4 dB below to 0.2 above the noise floor,

Figure 2. Signal-to-noise analyses of the simulated RH and RV channels. Error bars show the mean and the standard deviation of the selected samples in the RSa image in Figure 1a for a) 16 M, b) SC30M, and c) SC50M.
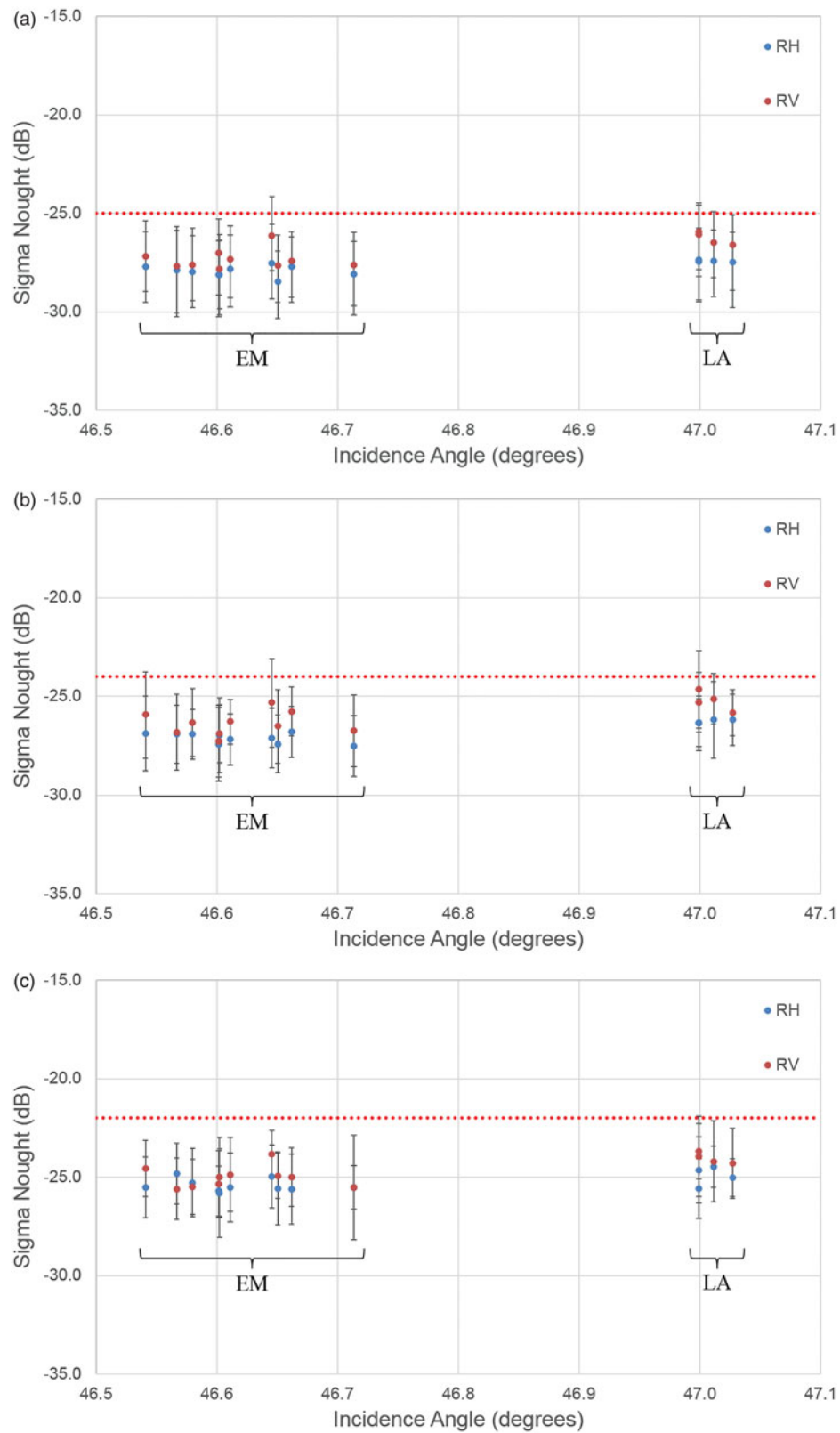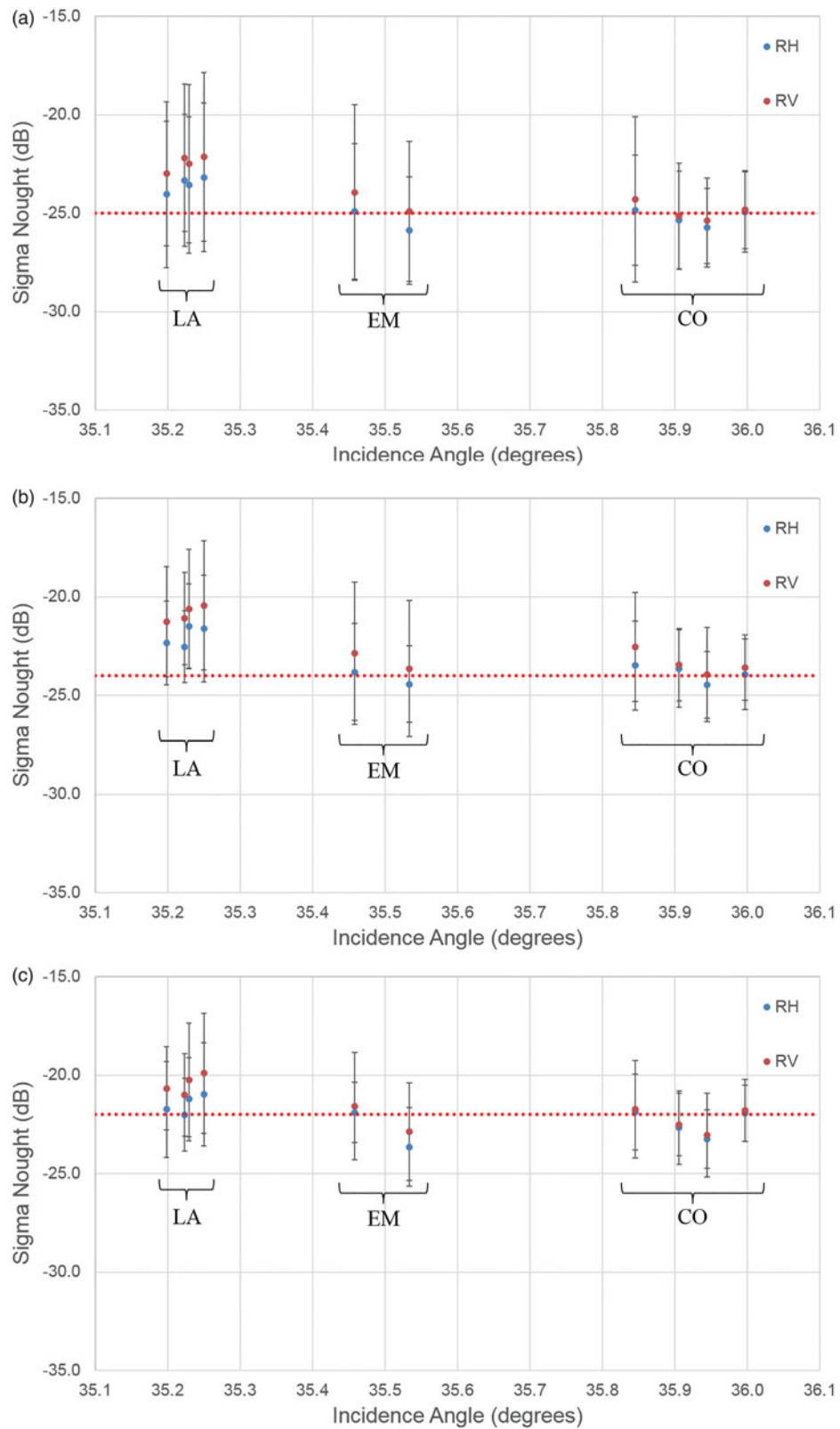
Figure 3. Signal-to-noise analyses of the simulated RH and RV channels. Error bars show the mean and the standard deviation of the selected samples in the RSb image in Figure 1b for a) 16 M, b) SC30M, and c) SC50M.

Table 4. Identified CP features with discrimination capabilities between LA and EM or CO in the RSb image for the three RCM modes.

		LA vs. EM						LA vs. CO			
16M	K-S	SC30M	K-S	SC50M	K-S	16M	K-S	SC30M	K-S	SC50M	K-S
m-δ_S	*0.541*	σ^0_{RH}	**0.713**	σ^0_{RH}	0.679	ρ_{RHRV}	**0.756**	ρ_{RHRV}	**0.821**	$\sigma^0_{RR}/\sigma^0_{RL}$	**0.854**
m-χ_odd	*0.538*	SV3	**0.706**	σ^0_{RL}	0.652	$\sigma^0_{RR}/\sigma^0_{RL}$	**0.756**	$\sigma^0_{RR}/\sigma^0_{RL}$	**0.820**	μ	**0.854**
SV3	*0.533*	$\sigma^0_{RR}/\sigma^0_{RL}$	0.692	SE_Int	0.644	μ	**0.756**	μ	**0.820**	ρ_{RHRV}	**0.848**
σ^0_{RL}	*0.531*	μ	0.692	SV0	0.644	m	**0.754**	m	**0.820**	m	**0.827**
$\sigma^0_{RR}/\sigma^0_{RL}$	*0.514*	ρ_{RHRV}	0.692	SV3	0.636	m-χ_odd	**0.734**	m-δ_S	**0.803**	SV3	**0.813**
μ	*0.514*	m-χ_odd	0.691	m-χ_odd	0.631	m-δ_S	**0.732**	m-χ_odd	**0.802**	m-χ_odd	**0.811**
SE_Int	*0.513*	σ^0_{RL}	0.688	m-δ_S	0.615	SV3	**0.728**	SV3	**0.799**	m-δ_S	**0.804**
SV0	*0.513*	SE_Pol	0.675	ρ_{RHRV}	0.605	SE_Pol	**0.700**	SE_Pol	**0.773**	SE_Pol	**0.789**
m	*0.513*	m-δ_S	0.674	SE_Pol	0.592	σ^0_{RL}	0.679	σ^0_{RL}	**0.763**	σ^0_{RL}	**0.734**
ρ_{RHRV}	*0.507*	SE_Int	0.674	$\sigma^0_{RR}/\sigma^0_{RL}$	0.587	SE_Int	0.598	SE_Int	0.698	SE_Int	0.583
		SV0	0.674	μ	0.587	SV0	0.598	SV0	0.698	SV0	0.583
		m	0.629	m	0.550	σ^0_{RV}	0.571	σ^0_{RV}	0.657	σ^0_{RV}	0.553
		σ^0_{RV}	0.573	σ^0_{RV}	0.545			σ^0_{RH}	0.626	α_s	0.553
								α_s	0.531		

Italic indicates CP features of moderate separability and bold indicates CP features of good separability.

whereas in the RV channel the mean values lie from 0.4–1.1 dB above the noise floor level (Figure 3b). In the CO regions, the mean values in the RH channel lie from 0.5 dB below to 0.5 dB above the noise floor level, whereas in the RV channel the mean values lie from 0.1–1.5 dB above the noise floor level (Figure 3b). Figure 3c shows the RH and RV mean values for LA, EM and CO in the SC50M mode. As for the 16 M and SC30M modes, the mean backscattering values of LA, EM, and CO in the RV channel are always higher than the mean values in the RH channel for the SC50M mode. Generally, we note in the SC50M mode that the mean values of LA and oil slicks are closer to the noise level of the mode compared to the 16 M and SC30M modes. The mean values for LA in the RH channel lie from 0.0–1.0 dB above the noise level and in the RV channel from 1.0–2.1 dB above the noise level. EM regions have mean signal values of 1.7 dB below to 0.1 dB above the noise level in the RH channel and 0.9 dB below to 0.4 dB above the noise level in the RV channel (Figure 3c). In the CO regions, the mean values in the RH channel lie from 1.3 dB below to 0.1 dB above the noise floor level, whereas in the RV channel the mean values lie from 1.0 dB below to 0.3 dB above the noise level (Figure 3c). We note from Figure 3 that mean signal values of LA is always higher than mean signal values of EM and CO in the three RCM modes. The results presented here indicate that simulated RH and RV channels in RSb image provide higher signal-to-noise ratios than the RSa image. Due to the high noise contamination observed in the RH and RV channels of the RSa image, our subsequence analysis in the next sections is confined to the RSb image.

Separability analysis

The discrimination between LA and oil slicks in the derived CP features of the RSb image is quantitatively evaluated using the collected samples (Figure 1b). Table 4 shows the identified CP features presenting discrimination capabilities between LA and the two mineral oil types sorted in a descending order in terms of their K-S distance. We highlight CP features of moderate separability between LA and EM or CO in italic. CP features of good separability are highlighted in bold.

For the 16 M mode, the identified CP features which present a potential separability between LA and EM are all of moderate separability. The highest K-S distance between LA and EM (0.541) is provided by the m-δ_S feature. Unlike the 16 M mode, the SC30M mode has among the identified CP features 2 with good separability between LA and EM, with the highest K-S distance (0.713) given by the σ^0_{RH} feature. The σ^0_{RH} feature is also the CP feature with the highest K-S distance between LA and EM (0.679) in the SC50M mode, but with moderate separability. Thus, similar to the 16 M mode, all the identified CP features in the SC50M mode are of moderate separability between LA and EM.

As shown in Table 4, the discrimination between LA and CO seems to be easier than the discrimination between LA and EM. This is evident from the fact that all the three RCM modes contain CP features with good separability. In the 16 M mode, the highest K-S distance between LA and CO (0.756) is given by the ρ_{RHRV} feature. This feature is also on the top of the list of features for discrimination capabilities between LA and CO in the SC30M mode, with K-S distance equal to 0.821. In the SC50M mode, the
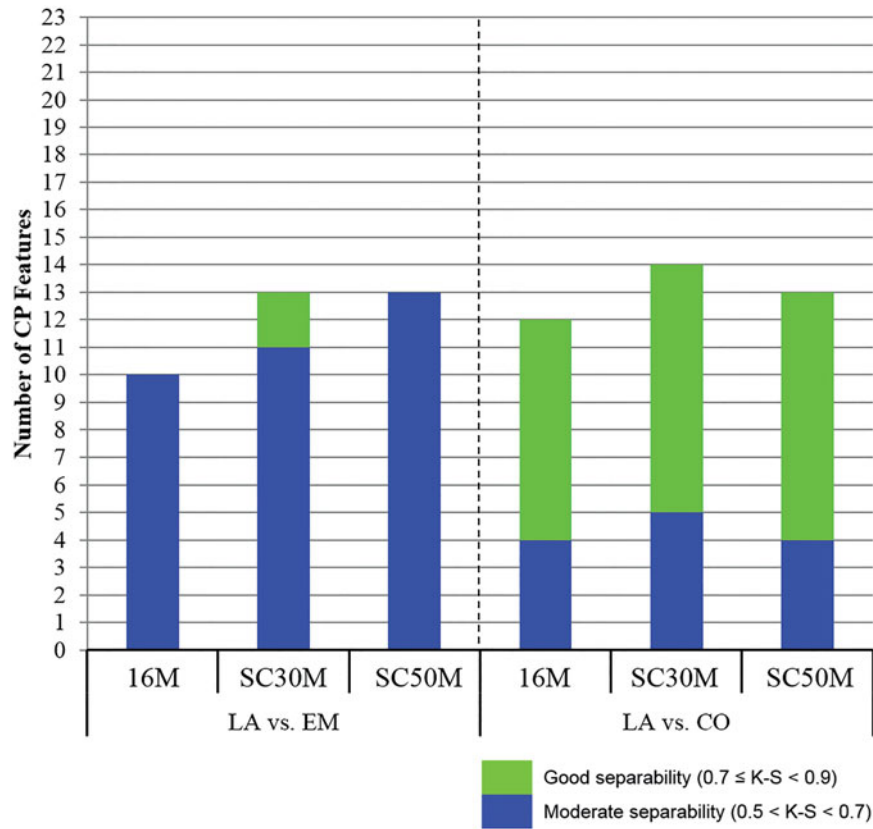
Figure 4. The change in the number of CP features with discrimination capabilities between LA and EM or CO within the 3 RCM modes in the RSb image.

highest K-S distance between LA and CO (0.854) is given by the $\sigma_{RR}^0/\sigma_{RL}^0$ feature. This feature is the second in terms of K-S distance values in the 16 M and SC30M modes (Table 4). It is worth stating that the assumption we make in this study that two sample sets (e.g. LA and EM) are separable in a CP feature if their K-S distance is >0.5, implies that we reject the null hypothesis that the two sample sets came from the same statistical distribution. This assumption should be valid for a defined alpha value (e.g. 0.05), given the large sample sizes we used for the calculation of the K-S distance. The 0.5 threshold value is an appropriate conservative cutoff, as smaller K-S distances could also lead to a rejection of the null hypothesis at the defined alpha value, given the large sample sizes.

Figure 4 shows the change in the number of identified CP features for both EM and CO between the three RCM modes. For the discrimination between LA and EM, the number of identified CP features in the 16 M mode is 10 (moderate separability only). This number becomes 13 in the SC30M and SC50M modes. However, two of the 13 identified CP features are of good separability only in the SC30M mode, while all the identified CP features in the SC50M are of moderate separability.

The number of identified CP features with discrimination capabilities between LA and CO for the 16 M mode is equal to 12, which is the lowest among the other RCM modes (Figure 4). From the identified 12 CP features, four are of moderate separability and eight are of good separability. The maximum number of identified CP features with discrimination capabilities between LA and CO is achieved in the SC30M mode (14 CP features), with 5 features being of moderate separability and 9 features being of good separability. The total number of identified CP features decreases to 13 in the SC50M mode, with 4 features being of moderate separability and 9 features being of good separability (Figure 4). The change in the number of identified CP features between the RCM modes could be due to the difference in spatial resolutions and noise floors. It is worth noting that for the 16 M and SC30M modes, all the CP features with discrimination capabilities between LA and EM can also separate LA and CO (Table 4). This is also valid for the SC50M mode, except for the σ_{RH}^0 feature which appears as the best CP feature for the discrimination between LA and EM (largest K-S distance), but fails in the SC50M mode in the separation between LA and CO (K-S distance <0.5). We also note for this

feature (σ_{RH}^0) that it provides discrimination capabilities between LA and CO only in the SC30M. This is because in the 16 M and SC50M modes the K-S distance between LA and CO was slightly below (0.476 and 0.487, respectively) the predefined threshold value of 0.5. It seems here that the K-S distance is mainly affected by both the noise floor and the spatial resolution of each RCM mode. The 16 M mode has the lowest noise floor (-25 dB) but the highest spatial resolution (16 m), while the SC50M has the highest noise floor (-22 dB) but the lowest spatial resolution (50 m). The SC30M is sort of a mode between the 16 M and the SC50M in terms of noise floor (-24 dB) and spatial resolution (30 m). This seems to allow the σ_{RH}^0 to slightly pass the threshold of 0.5 for the K-S distance.

Correlation analysis

Prior to the classification of LA and mineral oil slicks, the Spearman correlation between the identified CP features in Table 4 is calculated to detect correlated features and eliminate information redundancy. Figure 5 shows a representation of the Spearman correlation for the three RCM modes for the case of LA and EM (left-hand column) and for the case of LA and CO (right-hand column).

LA and EM

Figure 5a shows the Spearman correlation between the identified CP features of the 16 M mode. Based on the calculated Spearman correlation, two groups of strongly correlated CP features (≥ 0.90) are obtained. The two groups are shown in Table 5 with the CP features sorted in a descending order in terms of the K-S distance between LA and EM.

Figure 5b shows the Spearman correlation between the identified CP features of the SC30M mode. Based on the calculated Spearman correlation, four groups of strongly correlated features are obtained, which are presented in Table 5 with the CP features sorted in a descending order in terms of the K-S distance between LA and EM. Figure 5c shows the Spearman correlation between the identified CP features of the SC50M mode. Based on the calculated Spearman correlation, 3 groups of strongly correlated features are obtained, which are presented in Table 5 sorted in a descending order in terms of the K-S distance values. Furthermore, Table 5 shows that the σ_{RH}^0 feature is found less correlated with all the other CP features (< 0.9) in the SC50M mode.

LA and CO

The Spearman correlation coefficient was also calculated for the identified CP features of the 16M mode before the classification of LA and CO. Figure 5d presents a plot of the calculated correlation between all the identified CP features. Based on the obtained correlation 4 groups of highly correlated (≥ 0.90) CP features are created, as shown in Table 6.

Figure 5e shows the Spearman correlation between the identified CP features in the SC30M mode. Four groups of highly correlated CP features are obtained and shown in Table 6. Furthermore, two CP features (α_s and σ_{RH}^0) are found less correlated (< 0.90) with all the other CP features. For the SC50M, the obtained Spearman correlation between the identified CP features is shown in Figure 5f. Based on the calculated correlation, three groups of highly correlated CP features are obtained. Furthermore, the α_s feature is found less correlated with all the other CP features (< 0.9).

Data classification

Classification of LA and EM

As shown in Table 5, both CP feature groups in 16 M mode has the m-δ_S as the top CP feature with the highest K-S distance between LA and EM. Thus, the m-δ_S feature is selected and used for the classification of LA and EM. This feature is ingested in the SVM classification algorithm and the classification results of LA and EM for the 16 M mode are shown in Figure 6a. LA is assigned to the green class, while EM is assigned to the red class.

Also, the confusion matrix of the classification results is shown in Table 7. Herein, a high classification accuracy of 96.6% is achieved for the EM regions, while a low classification accuracy of 55.5% is obtained for the LA. The achieved overall classification accuracy is 63.6% with a Kappa coefficient equal to 0.314.

For the SC30M mode, a CP vector is created containing the σ_{RH}^0 and SV3 features, given the 4 groups of strongly correlated features in Table 5. This feature vector is ingested in the SVM classification algorithm and the classification results of LA and EM in the SC30M mode are shown in Figure 6b. Also, Table 7 shows the accuracy of the classification results. A lower classification accuracy of EM is obtained in the SC30M (80.5%) compared to the 16 M mode (96.6%). However, the classification accuracy of LA in the SC30M mode (95.5%) is found much higher than that of the 16 M mode (55.5%), with accuracy improvement of 40.0%. The SC30M mode achieved an overall
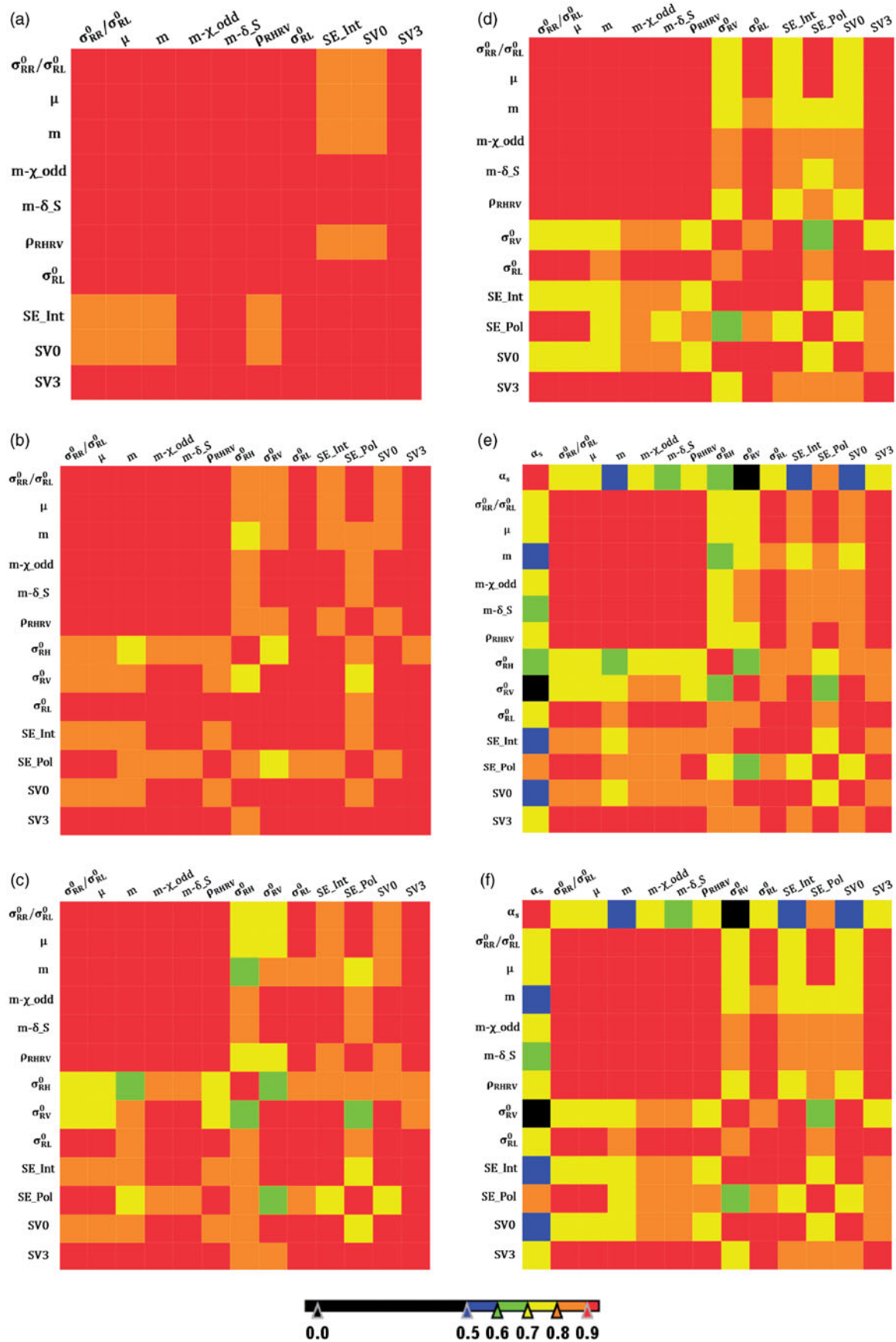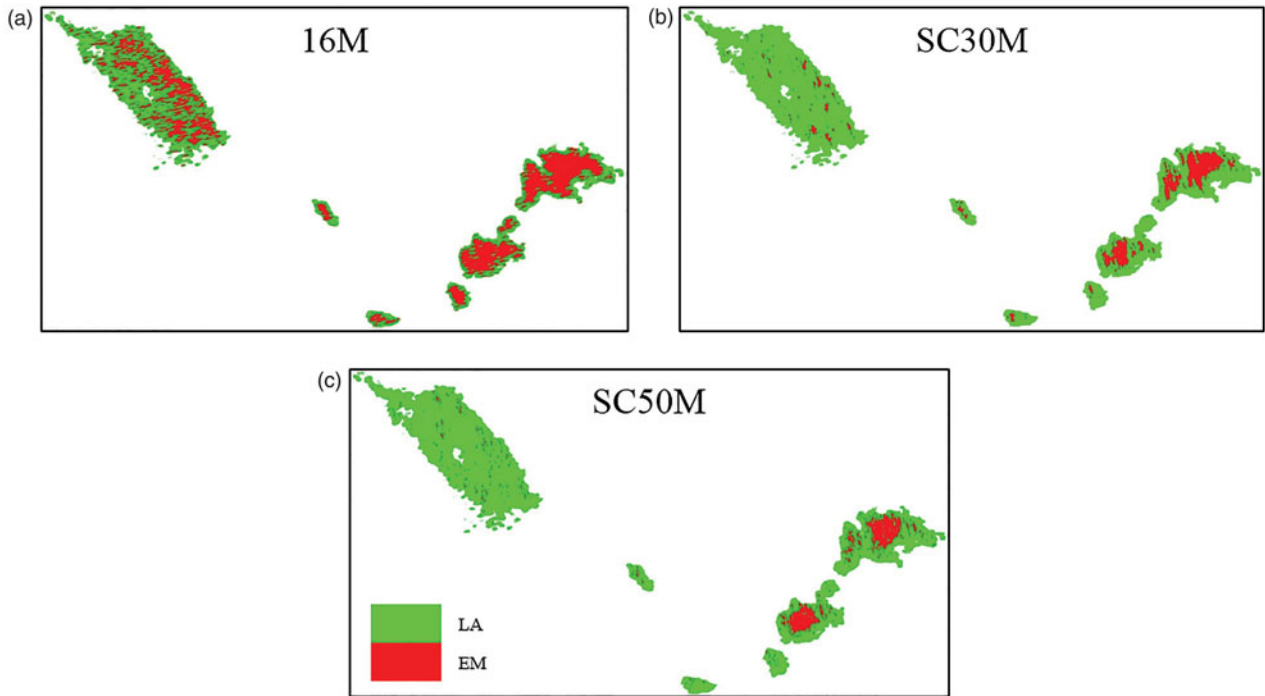
Figure 5. The Spearman correlation of the identified CP features with discrimination capabilities between LA and EM in RSb for a) 16 M, b) SC30M and c) SC50M modes. The Spearman correlation of the identified CP features with discrimination capabilities between LA and CO in RSb for d) 16 M, e) SC30M and f) SC50M modes.

Table 5. Groups of strongly correlated (R $\geq$ 0.90) CP features for each RCM mode in the RSb image for LA and EM.

16M		SC30M				SC50M			
Strongly Correlated CP Features		Strongly Correlated CP Features				Strongly Correlated CP Features			
Group#		Group#				Group#			
1	2	1	2	3	4	1	2	3	
m-δ_S	m-δ_S	SV3	σ^0_{RH}	SV3	SV3	SV3	σ^0_{RL}	SV3	σ^0_{RH}
m-χ_odd	m-χ_odd	$\sigma^0_{RR}/\sigma^0_{RL}$	σ^0_{RL}	m-χ_odd	$\sigma^0_{RR}/\sigma^0_{RL}$	m-χ_odd	SE_Int	ρ_{RHRV}	
SV3	SV3	μ	SE_Int	σ^0_{RL}	μ	m-δ_S	SV0	SE_Pol	
σ^0_{RL}	σ^0_{RL}	ρ_{RHRV}	SV0	m-δ_S	ρ_{RHRV}	ρ_{RHRV}	σ^0_{RV}	$\sigma^0_{RR}/\sigma^0_{RV}$	
$\sigma^0_{RR}/\sigma^0_{RL}$	SE_Int	m-χ_odd		SE_Int	SE_Pol	$\sigma^0_{RR}/\sigma^0_{RL}$		μ	
μ	SV0	σ^0_{RL}		SV0		μ			
m		m-δ_S		σ^0_{RV}		m			
ρ_{RHRV}		m							

Table 6. Groups of strongly correlated CP features for each RCM mode in the RSb image for LA and CO.

16M				SC30M						SC50M			
Strongly Correlated CP Features				Strongly Correlated CP Features						Strongly Correlated CP Features			
Group#				Group#						Group#			
1	2	3	4	1	2	3	4			1	2	3	
ρ_{RHRV}	σ^0_{RL}	$\sigma^0_{RR}/\sigma^0_{RL}$	SE_Int	ρ_{RHRV}	SE_Int	ρ_{RHRV}	σ^0_{RL}	α_s	σ^0_{RH}	$\sigma^0_{RR}/\sigma^0_{RL}$	σ^0_{RL}	SE_Int	α_s
$\sigma^0_{RR}/\sigma^0_{RL}$	SE_Int	μ	SV0	$\sigma^0_{RR}/\sigma^0_{RL}$	SV0	$\sigma^0_{RR}/\sigma^0_{RL}$	SE_Int			μ	SE_Int	SV0	
μ	SV0	SE_Pol	σ^0_{RV}	μ	σ^0_{RV}	μ	SV0			ρ_{RHRV}	SV0	σ^0_{RV}	
m				m		SV3				m			
m-χ_odd				m-δ_S		SE_Pol				SV3			
m-δ_S				m-χ_odd						m-χ_odd			
SV3				SV3						m-δ_S			

Figure 6. Classification of LA and EM in the a) 16 M, b) SC30M, and c) SC50M modes.

classification accuracy of 92.5% with a Kappa coefficient of 0.765, both much higher than the 16 M mode. For the SC50M mode, a CP vector is created containing the σ^0_{RL} and SV3 features from the 3 groups of strongly correlated CP features in Table 5. Also, the σ^0_{RH} feature (less correlated) is added to the created CP vector for the SVM classification. Figure 6c shows the classification results of the SC50M mode, with the obtained accuracy in Table 7. The classification accuracy of EM regions is 87.7% in the SC50M mode, which

is slightly higher than that of the SC30M (80.5%) but still lower than that of the 16 M mode (96.6%). Very high classification accuracy of LA (97.3%) is achieved in the SC50M mode, which is slightly higher than the achieved in the SC30M mode (95.5%), as indicated in Table 7. The overall classification accuracy of LA and EM in the SC50M mode is 95.4% (Kappa coefficient = 0.855), which is the highest compared to the 16 M and SC30M modes (Table 7).

The effect of the different spatial resolutions of the 3 RCM modes should be evident in the classification results shown in Figure 6. We note that the 16 M mode with its higher spatial resolution could detect successfully EM, with only a small zone around the EM edges misclassified as LA (green). However, due to the higher spatial resolution of that mode, some areas within the LA slicks were misclassified as EM probably due to properties more similar to EM. These could be areas with thicker film of plant oil. The lower resolution of the SC30M and SC50M has masked out almost all these areas within the LA slicks. Nevertheless, the lower spatial resolution of the SC30M and SC50M modes increased the green zone (misclassification as LA) around the EM edges. This misclassified green zone in the outermost part of EM regions is probably due to thinner film of EM over time (Skrunes et al. 2014).

From the results above, it seems that in terms of EM detection, the 16 M mode performs the best.

However, both SC30M and SC50M showed high overall performance, with the SC50M being slightly highest (Table 7).

Classification of LA and CO

From the created 4 groups in the case of 16 M mode (Table 6), a CP vector containing the ρ_{RHRV} and σ^0_{RL} features is formed and ingested in the SVM classification algorithm. It is worth mentioning that in order to perform the classification on the LA and CO and exclude the EM which is located in-between, we extracted the perimeters of the LA and CO slicks and used them as a mask in which the classification is applied. Figure 7a shows the classification results of LA and CO for the 16 M mode. Also, the resulting classification accuracy and Kappa coefficient are presented in Table 8.

As shown in Table 8, a high classification accuracy of 91.9% is achieved for the CO, while the LA is detected with a lower accuracy equal to 86.5%. The overall classification accuracy of LA and CO is equal to 89.6% with a Kappa coefficient equal to 0.788 (Table 8).

For the SC30M mode, a feature vector containing the less correlated CP features (Table 6) in addition to ρ_{RHRV} and σ^0_{RL} from the 4 groups of highly correlated features (Table 6) is formed and ingested in the SVM classification algorithm. Figure 7b shows the SC30M classification results of the LA and CO, with the obtained accuracy presented in Table 8. Herein, the

Table 7. CP features used for the LA and EM classification with the classification accuracy and Kappa coefficient for each RCM mode.

RCM Mode	CP Vector		Classification Accuracy (%)			
			LA	EM	Overall	Kappa
16M	m-δ_S	LA	55.5	3.4	63.6	0.314
		EM	44.5	96.6		
SC30M	σ^0_{RH} SV3	LA	95.5	19.5	92.5	0.765
		EM	4.5	80.5		
SC50M	σ^0_{RH} σ^0_{RL} SV3	LA	97.3	12.3	95.4	0.855
		EM	2.7	87.7		

Table 8. CP features used for the LA and CO classification with the classification accuracy and Kappa coefficient for each RCM mode.

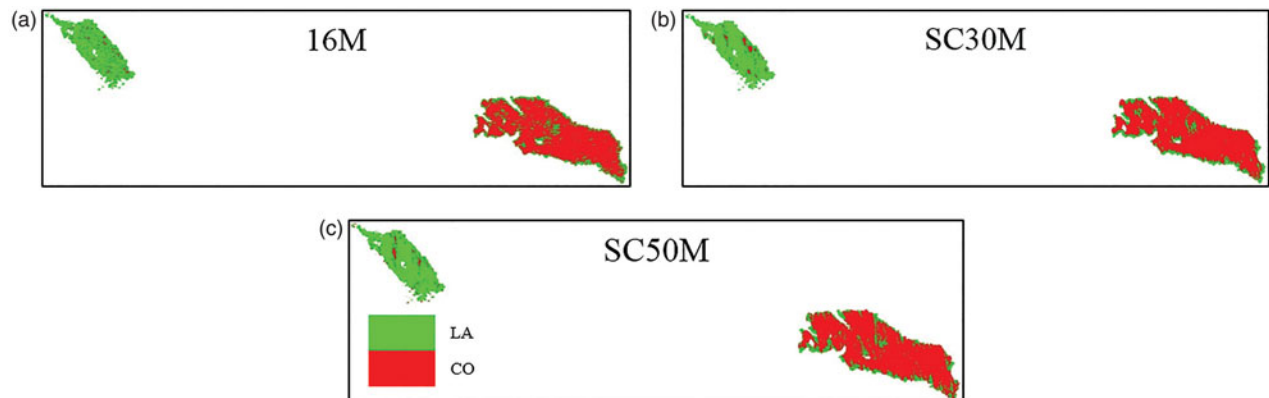| RCM Mode	CP Vector		Classification Accuracy (%)			
			LA	CO	Overall	Kappa
16M	ρ_{RHRV} σ^0_{RL}	LA	86.5	8.1	89.6	0.788
		CO	13.5	91.9		
SC30M	ρ_{RHRV} σ^0_{RL} α_s σ^0_{RH}	LA	93.5	4.5	94.6	0.891
		CO	6.5	95.5		
SC50M	$\sigma^0_{RR}/\sigma^0_{RL}$ σ^0_{RL} α_s	LA	95.5	2.3	96.7	0.934
		CO	4.5	97.7		

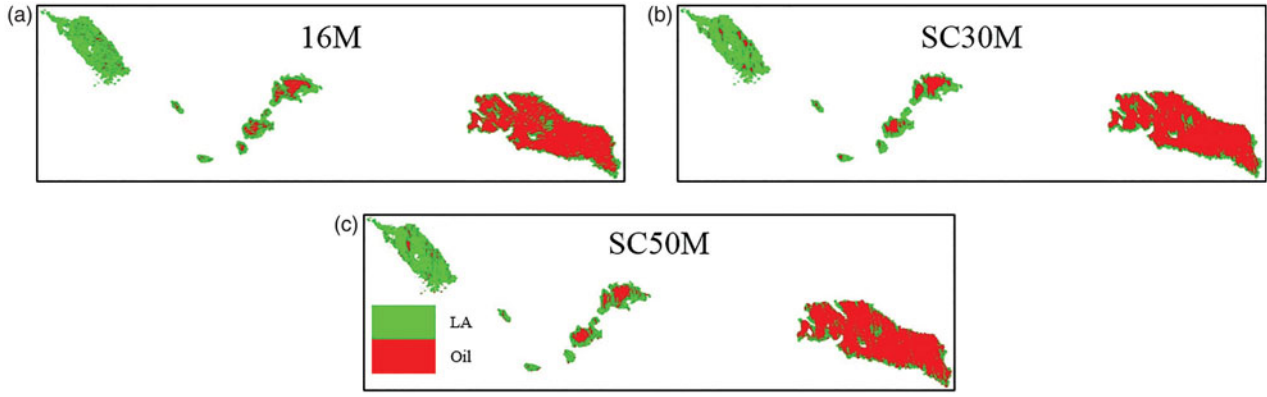**Figure 7.** Classification of LA and CO in the a) 16 M, b) SC30M, and c) SC50M modes.

Figure 8. Classification of LA and oil slicks (EM and CO) in the a) 16 M, b) SC30M, and c) SC50M modes.

classification accuracy of both LA and CO (93.5% and 95.5%, respectively) is higher than that of 16 M mode. The overall classification accuracy of LA and CO is equal to 94.6%, with a Kappa coefficient of 0.891.

For the SC50M mode, a CP vector containing the $\sigma_{RR}^0/\sigma_{RL}^0$, σ_{RL}^0 and α_s features (Table 6) is created and ingested in the SVM classification algorithm. Table 8 shows the accuracy of the classification results shown in Figure 7c. In the SC50M mode, both LA and CO achieve the highest classification accuracy (95.5% and 97.7%, respectively), as shown in Table 8. This accuracy is slightly higher than that of the SC30M and much higher than that of the 16 M mode (Table 8). Thus, the highest overall accuracy is achieved in the SC50M mode and reaches the 96.7% (Kappa = 0.934), which is slightly higher than that of the SC30M (94.6%).

From the results above for all examined modes, it seems that in terms of overall performance the SC30M and SC50M showed high performance, with the SC50M being slightly higher (Table 8).

Classification of LA and oil

Herein, we attempt to discriminate between LA and all the mineral oil slicks (EM and CO) in the experimental site using the SVM classification algorithm. In each mode, we use for the classification the CP features in both feature vectors shown in Table 7 and 8. In the 16 M mode, the CP vector used for the classification of LA and EM contains the m-δ_S feature, which is highly correlated with the ρ_{RHRV} feature contained in the CP vector used for the classification of LA and CO. Thus, we excluded the m-δ_S feature and used for the classification of LA and mineral oil slicks the CP vector in Table 8. Figure 8a shows the classification results of LA and oil slicks. Also, the accuracy of the classification results is shown in Table 9. The LA and oil slicks are classified with accuracy equal to 86.2% and 87.6%, respectively. The achieved overall

Table 9. CP features used for the LA and oil slicks (EM and CO) classification with the classification accuracy and Kappa coefficient for each RCM mode.

RCM Mode	CP Vector		Classification Accuracy (%)			
			LA	Oil	Overall	Kappa
16M	ρ_{RHRV} σ_{RL}^0	LA	86.2	12.4	87.1	0.733
		Oil	13.8	87.6		
SC30M	ρ_{RHRV} σ_{RL}^0 α_s σ_{RH}^0	LA	93.9	9.5	92.6	0.845
		Oil	6.1	90.5		
SC50M	$\sigma_{RR}^0/\sigma_{RL}^0$ σ_{RL}^0 σ_{RH}^0 α_s	LA	94.0	3.1	95.8	0.911
		Oil	6.0	96.9		

classification accuracy and Kappa coefficient are equal to 87.1% and 0.733, respectively.

In the SC30M mode, the CP vector used for the classification of LA and EM contains two features; σ_{RH}^0 and SV3 (Table 7). The first feature (σ_{RH}^0) is also one of the elements of the CP vector used for the classification of LA and CO, while the second feature (SV3) is highly correlated with the ρ_{RHRV} feature (Table 8). Thus, the CP vector used for the classification of LA and oil slicks in the SC30M is identical to the CP vector used for the classification of LA and CO in the same mode. Figure 8b shows the classification results of LA and oil slicks in the SC30M mode, while in Table 9 the achieved accuracy is presented. As shown in Table 9, higher classification accuracy is obtained for both LA (93.9%) and oil slicks (90.5%) in the SC30M compared to the 16 M mode. Therefore, higher overall classification accuracy (92.6%) and Kappa coefficient values (0.845) are achieved in this mode.

In the SC50M mode, the CP vector used for the classification of LA and EM contains 3 features; σ_{RH}^0, σ_{RL}^0 and SV3 (Table 7). The second feature (σ_{RL}^0) is also one of the elements of the CP vector used for the classification of LA and CO (Table 8), while the third (SV3) is highly correlated with the $\sigma_{RR}^0/\sigma_{RL}^0$ feature (Table 6). Thus, the CP vector used for the classification of LA and oil slicks in the SC50M includes the features of the CP vector used for the classification of

Table 10. Summary of the classification accuracy of LA and oil slicks in our study and Skrunes et al. (2014).

	Classification Accuracy (%)											
	16M		SC30M		SC50M		$\log(\gamma_{co})$		$\log(\mu)$		$\log(\gamma_{co})+\log(\mu)$	
	LA	Oil	LA	Oil	LA	Oil	LA	Oil	LA	Oil	LA	Oil
LA	86.2	12.4	93.9	9.5	94.0	3.1	99.8	27.2	98.6	20.9	99.0	21.8
Oil	13.8	87.6	6.1	90.5	6.0	96.9	0.2	72.8	1.4	79.1	1.0	78.2
Overall Accuracy	87.1		92.6		95.8		79.8		84.1		83.6	

LA and CO in the same mode, in addition to the σ^0_{RH} feature. Figure 8c shows the classification results of LA and oil slicks, while in Table 9 the achieved accuracy is presented. Classification accuracy of LA in the SC50M mode (94.0%) is approximately equal to that of the SC30M mode (93.9%). Furthermore, the highest classification accuracy of oil slicks (96.9%) is achieved in the SC50M mode, which is slightly higher than that of the SC30M mode (90.5%). Consequently, highest overall classification accuracy and Kappa coefficient (95.8% and 0.911, respectively) are obtained in the SC50M mode, and are slightly higher than that of the SC30M mode (92.6% and 0.845, respectively).

Comparison with Co-polarization SAR results

It would be of interest for our study to compare the obtained classification results using the simulated RCM CP SAR data for LA and mineral oil slicks with those reported in Skrunes et al. (2014) using polarimetric features derived from the copolarization channels (HH and VV) of the RSb image. It is worth mentioning that Skrunes et al. (2014) considered only the classification of LA and all mineral oil slicks as one class. Unlike our study, the separate classification of LA and EM or LA and CO in the RSb SAR image was not tested in Skrunes et al. (2014). In Skrunes et al. (2014), the classification of LA and oil slicks was performed using: (1) the logarithm of the copolarization power ratio ($\log(\gamma_{co})$), (2) the logarithm of the geometric intensity ($\log(\mu)$), and (3) both $\log(\gamma_{co})$ and $\log(\mu)$.

As shown in Table 10, the classification accuracy of LA in the 3 experiments conducted in Skrunes et al. (2014) is slightly higher than that of the SC30M and SC50M, but much higher than that of the 16 M. In contrary, the classification accuracy of the mineral oil slicks in all RCM modes is much higher than that obtained in the 3 experiments of Skrunes et al. (2014).

In terms of overall classification performance, Table 10 shows that the classification performance of the examined RCM modes in our study is better than that reported in Skrunes et al. (2014), especially for the case of SC30M and SC50M modes. The observed higher overall performance of the RCM modes is noted, though the polarimetric features used for the classification of LA and mineral oil slicks in Skrunes

et al. (2014) were obtained from dual polarized SAR imagery with lower noise contamination (RADARSAT-2 noise floor was between −32 dB and −35 dB), compared to the CP features in our study which were obtained from simulated RCM data with higher noise floor (between −22 dB and −25 dB). The higher information content of the CP SAR data against the conventional dual polarized SAR data should have contributed to the observed higher performance. Another factor should be the classification algorithm which we used in our study compared to the one used in Skrunes et al. (2014). An unsupervised k-means classification approach was adopted by Skrunes et al. (2014), where k numbers of class centers are randomly selected and the classification is iteratively performed based on the minimum Euclidean distance. In our case, we performed a supervised classification using the SVM algorithm, which is a sophisticated machine learning classification algorithm with well-known better performance.

It is worth mentioning that in Zhang et al. (2017), ten CP features were extracted from simulated CP SAR data obtained from the RSb image. These features were used for the classification of mineral oil using SVM classification. The overall classification accuracy was 95.2%, which is higher than the obtained overall classification in the 16 M and SC30M (87.1% and 92.6%, respectively), but slightly lower than the obtained overall classification accuracy of the SC50M (95.8%). However, it is important to emphasize the difference between our study and that by Zhang et al. (2017), which lies on the fact that in our study the focus is on the discrimination between LA and mineral oil slicks, while in Zhang et al. (2017) the focus was on the detection of mineral oil slicks by discriminating them from a class which included both clean sea and LA.

Discussion

CP features calculated from simulated SAR data of the RCM MR SAR modes could be utilized for the classification of LA and mineral oil slicks (EM and/or CO). Within the limited number of acquired SAR images for this oil release experiment, results in this study proved that the performance of the 3 RCM modes in

the discrimination and the subsequent classification of mineral oil slick varies between the 3 modes. As expected, this variation in the performance is not a function of the nominal noise floor only, but also the spatial resolution of each mode. This explains the fact that in our study the 16 M mode had the weakest performance compared to the other two modes, though it has the lowest nominal noise floor (-25 dB).

We note from Table 5 and 6 that the discrimination between LA and mineral oil spills is achieved using CP features associated mainly with the surface scattering mechanism and the power of the backscattered signals. This agrees with the literature where biogenic oil (i.e. LA) was found to exhibit surface scattering mechanism close to the Bragg scattering from the clean sea surface, while scattering from mineral oil is characterized by higher randomness process (Skrunes et al. 2014; Nunziata et al. 2008; Migliaccio et al. 2007). Also, the power of the backscattered signal from the biogenic oil is higher than that from mineral oil slicks.

In Table 7, we note that the 3 sets of CP features corresponding to the 3 modes are not identical. However, they are in many cases highly correlated. For example, the σ^0_{RL} in the SC50M mode and the SV3 in both SC30M and SC50M modes (Table 7) are highly correlated features with the m-δ_S feature in the 16 M mode (Table 5). Furthermore, the σ^0_{RL} feature in the SC50M is also one of the features highly correlated with the σ^0_{RH} in the SC30M (Table 5). The σ^0_{RH} in SC30M and SC50M (Table 5) is an exception since in the 16 M mode it is not correlated with any of the two feature groups in Table 5. In Table 8, we note that the ρ_{RHRV} and σ^0_{RL} features are common in the 3 modes, except for the SC50M where the ρ_{RHRV} is replaced with the $\sigma^0_{RR}/\sigma^0_{RL}$ feature, with which it is highly correlated (Table 6). The α_s is common in both SC30M and SC50M modes only, while σ^0_{RH} is unique in the SC30M (Table 8).

For the operational marine pollution monitoring, it is preferable to identify a single set of CP features consistent across the RCM MR modes and suitable for the discrimination and classification of mineral oil slicks. Thus, in terms of consistency, we note in Table 4 that all the identified CP features with discrimination capabilities between LA and mineral oil slicks (EM and CO) in the 16 M mode are common with the SC30M and SC50M modes.

Conclusions

All the medium resolution modes of the recently launched RCM are investigated for their expected potential in the discrimination between LA and different mineral oil slicks using simulated data. A noise analysis of the simulated data suggested that the feasibility of oil slick detection might not be possible at large radar incidence angles due to the backscattering in the RH and RV channels which could be lower than the nominal noise level. Results of the discrimination between LA and mineral oil slicks at steeper radar incidence angle (RSb image) showed that the SC50M mode provides the highest overall performance in term of LA and oil slicks (EM and/or CO) classification. This performance was slightly higher than that of the SC30M mode. Furthermore, results showed that the discrimination between LA and CO could be easier than the discrimination between LA and EM in the 3 modes. This is because the overall classification accuracy was always higher in the case of LA and CO. We should acknowledge that further research work is still required to confirm the above results using real RCM imagery with their induced speckle noise acquired under wide range of radar incidence angles. Furthermore, validation of the results with the suggested parameterization of this study is also needed over all types of oil slicks and lookalike phenomena (e.g. upwelling, ship wake, low wind, etc.) and under different environmental conditions (e.g. wind speed).

Acknowledgments

References

Alpers, W., Holt, B., and Zeng, K. 2017. "Oil spill detection by imaging radars: Challenges and pitfalls." *Remote Sensing of Environment*, Vol. 201: pp. 133–147. doi:10.1016/j.rse.2017.09.002.

Angelliaume, S., Dubois-Fernandez, P., Jones, C., Holt, B., Minchew, B., Amri, E., and Miegebielle, V. 2018. "SAR imagery for detecting sea surface slicks: performance assessment of polarization-dependent parameters." *IEEE Transactions on Geoscience and Remote Sensing*, Vol. 56(No. 8): pp. 4237–4257. doi:10.1109/TGRS.2018.2803216.

Apel, J. R., and Jackson, C. R. 2004. Synthetic Aperture Radar: Marine User's Manual. U.S. Department of Commerce, ISBN 9780160732140.

Brekke, C., and Solberg, A.H.S. 2005. "Oil spill detection by satellite remote sensing." *Remote Sensing of Environment*, Vol. 95(No. 1): pp. 1–13. doi:10.1016/j.rse.2004.11.015.

Buono, A., Nunziata, F., Migliaccio, M., and Li, X. 2016a. "Polarimetric analysis of compact-polarimetry SAR architectures for sea oil slick observation." *IEEE Transactions*

on *Geoscience and Remote Sensing*, Vol. 54(No. 10): pp. 5862–5874. doi:10.1109/TGRS.2016.2574561.

Buono, A., Nunziata, F., and Migliaccio, M. 2016b. "Analysis of full and compact polarimetric SAR features over the sea surface." *IEEE Geoscience and Remote Sensing Letters*, Vol. 13(No. 10): pp. 1527–1531. doi:10.1109/LGRS.2016.2595058.

Buono, A., Nunziata, F., de Macedo, C.R., Velotto, D., and Migliaccio, M. 2018. "A sensitivity analysis of the standard deviation of the copolarized phase difference for sea oil slick observation." *IEEE Transactions on Geoscience and Remote Sensing*, Vol. 57(No. 4): pp. 2022–2030. doi:10.1109/TGRS.2018.2870738.

Burges, C.J. 1998. "A tutorial on support vector machines for pattern recognition." *Data Mining and Knowledge Discovery*, Vol. 2(No. 2): pp. 121–167. doi:10.1023/A:1009715923555.

Charbonneau, F., Brisco, B., Raney, K., McNairn, H., Liu, C., Vachon, P., Shang, J., et al. 2010. "Compact polarimetry overview and applications assessment." *Canadian Journal of Remote Sensing*, Vol. 36(No. sup2): pp. S298–S315. doi:10.5589/m10-062.

Cheng, Y., Liu, B., Li, X., Nunziata, F., Xu, Q., Ding, X., Migliaccio, M., and Pichel, W. 2014. "Monitoring of oil spill trajectories with COSMO-skymed X-band SAR images and model simulation." *IEEE Journal of Selected Topics in Applied Earth Observations and Remote Sensing*, Vol. 7(No. 7): pp. 2895–2901. doi:10.1109/JSTARS.2014.2341574.

Cloude, S.R., Goodenough, D.G., and Chen, H. 2012. "Compact decomposition theory." *IEEE Geoscience and Remote Sensing Letters*, Vol. 9(No. 1): pp. 28–32. doi:10.1109/LGRS.2011.2158983.

Collins, M.J., Denbina, M., Minchew, B., Jones, C.E., and Holt, B. 2015. "On the use of simulated airborne compact polarimetric SAR for characterizing oil–water mixing of the deepwater horizon oil spill." *IEEE Journal of Selected Topics in Applied Earth Observations and Remote Sensing*, Vol. 8(No. 3): pp. 1062–1077. doi:10.1109/JSTARS.2015.2401041.

Dabboor, M., and Geldsetzer, T. 2014. "Towards sea ice classification using simulated RADARSAT constellation mission compact polarimetric SAR imagery." *Remote Sensing of Environment*, Vol. 140: pp. 189–195. doi:10.1016/j.rse.2013.08.035.

Dabboor, M., Iris, S., and Singhroy, V. 2018a. "The RADARSAT constellation mission in support of environmental applications." *Proceedings*, Vol. 2(No. 7): pp. 323. doi:10.3390/ecrs-2-05136.

Dabboor, M., Montpetit, B., Howell, S., and Haas, C. 2017. "Improving sea ice characterization in dry ice winter conditions using polarimetric parameters from C- and L-band SAR data." *Remote Sensing*, Vol. 9(No. 12): pp. 1270. doi:10.3390/rs9121270.

Dabboor, M., Montpetit, B., and Howell, S. 2018b. "Assessment of the high resolution SAR mode of the RADARSAT constellation mission for first year ice and multiyear ice characterization." *Remote Sensing*, Vol. 10(No. 4): pp. 594. doi:10.3390/rs10040594.

Desbordes, P., Ruan, S., Modzelewski, R., Pineau, P., Vauclin, S., Gouel, P., Michel, P., Di Fiore, F., Vera, P., and Gardin, I. 2017. "Predictive value of initial FDG-PET features for treatment response and survival in esophageal cancer patients treated with chemo-radiation therapy using a random forest classifier." *Plos One*, Vol. 12(No. 3): pp. e0173208. doi:10.1371/journal.pone.0173208.

Duda, R., Hart, P., and Stork, D. 2000. *Pattern Classification*. 2nd ed. New York: John Wiley & Sons. ISBN 978-0471056690.

Espeseth, M.M., Skrunes, S., Jones, C.E., Brekke, C., Holt, B., and Doulgeris, A.P. 2017. "Analysis of evolving oil spills in full-polarimetric and hybrid-polarity SAR." *IEEE Transactions on Geoscience and Remote Sensing*, Vol. 55(No. 7): pp. 4190–4210. doi:10.1109/TGRS.2017.2690001.

Fingas, M., and Brown, C.E. 2018. "A review of oil spill remote sensing." *Sensors*, Vol. 18(No. 2): pp. 91. doi:10.3390/s18010091.

Geldsetzer, T., Arkett, M., Zagon, T., Charbonneau, F., Yackel, J., and Scharien, R. 2015. "All-season compact-polarimetry C-band SAR observations of sea ice." *Canadian Journal of Remote Sensing*, Vol. 41(No. 5): pp. 485–504. doi:10.1080/07038992.2015.1120661.

Kumar, L.J.V., Kishore, J.K., and Rao, P.K. 2014. "Decomposition methods for detection of oil spills based on RISAT-1 SAR images." *International Journal of Remote Sensing & Geoscience*, Vol. 3(No. 4): pp. 1–10. ISSN No: 2319-3484.

Lee, J. S., and Pottier, E. 2009. *Polarimetric Radar Imaging: From Basics to Applications*. Boca Raton, Florida: CRC Press. ISBN 978-1420054972.

Li, H.Y., Perrie, W., Zhou, Y.Z., and He, Y.J. 2016. "Oil spill detection on the ocean surface using hybrid polarimetric SAR imagery." *Science China Earth Sciences*, Vol. 59(No. 2): pp. 249–257. doi:10.1007/s11430-015-5152-0.

Li, Y., Lin, H., Zhang, Y., and Chen, J. 2015. "Comparisons of circular transmit and linear receive compact polarimetric SAR features for oil slicks discrimination." *Journal of Sensors*, Vol. 2015: pp. 1. doi:10.1155/2015/631561.

Marghany, M., and Hashim, M. 2011. "Discrimination between oil spill and look-alike using fractal dimension algorithm from RADARSAT-1 SAR and AIRSAR/POLSAR data." *International Journal of Physical Sciences*, Vol. 6(No. 7): pp. 1711–1719. doi:10.5897/IJPS11.213.

Migliaccio, M., Nunziata, F., and Buono, A. 2015. "SAR polarimetry for sea oil slick observation." *International Journal of Remote Sensing*, Vol. 36(No. 12): pp. 3243–3273. doi:10.1080/01431161.2015.1057301.

Migliaccio, M., Gambardella, A., and Tranfaglia, M. 2007. "SAR polarimetry to observe oil spills." *IEEE Transactions on Geoscience and Remote Sensing*, Vol. 45(No. 2): pp. 506–511. doi:10.1109/TGRS.2006.888097.

Minchew, B., Jones, C., and Holt, B. 2012. "Polarimetric analysis of backscatter from the deepwater horizon oil spill using L-band synthetic aperture radar." *IEEE Transactions on Geoscience and Remote Sensing*, Vol. 50(No. 10): pp. 3812–3830. doi:10.1109/TGRS.2012.2185804.

Misra, T., Rana, S.S., Desai, N.M., Dave, D.B., Rajeevjyoti, Arora, R.K., Rao, C.N., Bakori, B.V., Neelakantan, R.S., and Vachchani, J.G. 2013. "Synthetic aperture radar payload on-board RISAT-1: configuration, technology and performance." *Current Science*, Vol. 104(No. 4): pp. 446–461.

Nord, M.E., Ainsworth, T.L., Lee, J.S., and Stacy, N.J.S. 2009. "Comparison of compact polarimetric synthetic

aperture radar modes." *IEEE Transactions on Geoscience and Remote Sensing*, Vol. 47(No. 1): pp. 174–188. doi:10.1109/TGRS.2008.2000925.

Nunziata, F., Gambardella, A., and Migliaccio, M. 2008. "On the Mueller scattering matrix for SAR sea oil slick observation." *IEEE Geoscience and Remote Sensing Letters*, Vol. 5(No. 4): pp. 691–695. doi:10.1109/LGRS.2008.2003127.

Nunziata, F., Migliaccio, M., and Li, X. 2015. "Sea oil slick observation using hybrid-polarity SAR architecture." *IEEE Journal of Oceanic Engineering*, Vol. 40(No. 2): pp. 426–440. doi:10.1109/JOE.2014.2329424.

Nunziata, F., de Macedo, C.R., Buono, A., Velotto, D., and Migliaccio, M. 2019. "On the analysis of a time series of X–band TerraSAR–X SAR imagery over oil seepages." *International Journal of Remote Sensing*, Vol. 40(No. 9): pp. 3623–3646. doi:10.1080/01431161.2018.1547933.

Press, W., Teukolsky, S. A., Vetterling, W., and Flannery, B. 2007. *Numerical Recipes, The Art of Scientific Computing.* 3rd ed. Cambridge: Cambridge University Press. ISBN 0-521-88068-8.

Raney, R.K., Cahill, J.T.S., Patterson, G.W., and Bussey, D.B. 2012. "The m-chi decomposition of hybrid dual-polarimetric radar data with application to lunar craters." *Journal of Geophysical Research*, Vol. 117(No. E12): pp. E00H21. doi:10.1029/2011JE003986.

Raney, R.K. 2007. "Hybrid-polarity SAR architecture." *IEEE Transactions on Geoscience and Remote Sensing*, Vol. 45(No. 11): pp. 3397–3404. doi:10.1109/TGRS.2007.895883.

Réfrégier, P., and Morio, J. 2006. "Shannon entropy of partially polarized and partially coherent light with Gaussian fluctuations." *Journal of the Optical Society of America A*, Vol. 23(No. 12): pp. 3036–3044. doi:10.1364/JOSAA.23.003036.

Salberg, A., Rudjord, Ø., and Solberg, A.H.S. 2014. "Oil spill detection in hybrid-polarimetric SAR images." *IEEE Transactions on Geoscience and Remote Sensing*, Vol. 52(No. 10): pp. 6521–6533. doi:10.1109/TGRS.2013.2297193.

Sabry, R., and Vachon, P.W. 2014. "A unified framework for general compact and quad polarimetric sar data and imagery analysis." *IEEE Transactions on Geoscience and Remote Sensing*, Vol. 52(No. 1): pp. 582–602. doi:10.1109/TGRS.2013.2242479.

Shirvany, R., Chabert, M., and Tourneret, J. 2012. "Ship and oil-spill detection using the degree of polarization in linear and hybrid/compact dual-pol SAR." *IEEE Journal of Selected Topics in Applied Earth Observations and Remote Sensing*, Vol. 5(No. 3): pp. 885–892. doi:10.1109/JSTARS.2012.2182760.

Singha, S., Ressel, R., Velotto, D., and Lehner, S. 2016. "A combination of traditional and polarimetric features for oil spill detection using TerraSAR-X." *IEEE Journal of Selected Topics in Applied Earth Observations and Remote Sensing*, Vol. 9(No. 11): pp. 4979–4990. doi:10.1109/JSTARS.2016.2559946.

Singha, S., Bellerby, T.J., and Trieschmann, O. 2013. "Satellite oil spill detection using artificial neural networks." *IEEE Journal of Selected Topics in Applied Earth Observations and Remote Sensing*, Vol. 6(No. 6): pp. 2355–2363. doi:10.1109/JSTARS.2013.2251864.

Singha, S., Velotto, D., and Lehner, S. 2014. "Near real time monitoring of platform sourced pollution using TerraSAR-X over the North Sea." *Marine Pollution Bulletin*, Vol. 86(No. 1–2): pp. 379–390. doi:10.1016/j.marpolbul.2014.06.041.

Skrunes, S., Brekke, C., Eltoft, T., and Kudryavtsev, V. 2015. "Comparing near-coincident C- and X-band SAR acquisitions of marine oil spills." *IEEE Transactions on Geoscience and Remote Sensing*, Vol. 53(No. 4): pp. 1958–1975. doi:10.1109/TGRS.2014.2351417.

Skrunes, S., Brekke, C., and Eltoft, T. 2014. "Characterization of marine surface slicks by Radarsat-2 multipolarization features." *IEEE Transactions on Geoscience and Remote Sensing*, Vol. 52(No. 9): pp. 5302–5319. doi:10.1109/TGRS.2013.2287916.

Skrunes, S., Brekke, C., Jones, C., Espeseth, M., and Holt, B. 2018. "Effect of wind direction and incidence angle on polarimetric SAR observations of slicked and unslicked sea surfaces." *Remote Sensing of Environment*, Vol. 213: pp. 73–91. doi:10.1016/j.rse.2018.05.001.

Topouzelis, K., and Psyllos, A. 2012. "Oil spill feature selection and classification using decision tree forest on SAR image data." *ISPRS Journal of Photogrammetry and Remote Sensing*, Vol. 68: pp. 135–143. doi:10.1016/j.isprsjprs.2012.01.005.

Topouzelis, K. 2008. "Oil spill detection by SAR images: dark formation detection, feature extraction and classification algorithms." *Sensors*, Vol. 8(No. 10): pp. 6642–6659. doi:10.3390/s8106642.

Truong-Loi, M., Freeman, A., Dubois-Fernandez, P., and Pottier, E. 2009. "Estimation of soil moisture and Faraday rotation from bare surfaces using compact polarimetry." *IEEE Transactions on Geoscience and Remote Sensing*, Vol. 47(No. 11): pp. 3608–3615. doi:10.1109/TGRS.2009.2031428.

Vijayakumar, S., and Santhi, V. 2015. "Oil spill detection in SAR images - A review." *International Journal of Oceans and Oceanography*, Vol. 9(No. 2): pp. 221–228. ISSN 0973-2667.

Yin, J., Yang, J., Zhou, Z., and Song, J. 2015. "The extended Bragg scattering model-based method for ship and oil-spill observation using compact polarimetric SAR." *IEEE Journal of Selected Topics in Applied Earth Observations and Remote Sensing*, Vol. 8(No. 8): pp. 3760–3772. doi:10.1109/JSTARS.2014.2359141.

Yin, J., Moon, W., and Yang, J. 2015. "Model-based pseudo-quad-pol reconstruction from compact polarimetry and its application to oil-spill observation." *Journal of Sensors*, Vol. 2015: pp. 1. doi:10.1109/JSTARS.2014.2359141.

Zhang, B., Li, X., Perrie, W., and Garcia-Pineda, O. 2017. "Compact polarimetric synthetic aperture radar for marine oil platform and slick detection." *IEEE Transactions on Geoscience and Remote Sensing*, Vol. 55(No. 3): pp. 1407–1423. doi:10.1109/TGRS.2016.2623809.

Zhang, B., Perrie, W., Li, X., and Pichel, W.G. 2011. "Mapping sea surface oil slicks using RADARSAT-2 quad-polarization SAR image." *Geophysical Research Letters*, Vol. 38(No. 10): L10602. doi:10.1029/2011GL047013.

Zhang, Y., Li, Y., Liang, X.S., and Tsou, J. 2017. "Comparison of oil spill classifications using fully and compact polarimetric SAR images." *Applied Sciences*, Vol. 7(No. 2): pp. 193. doi:10.3390/app7020193.